

The statistical evolution of a stratified mixing layer with horizontal shear invoking feature extraction

Eric Arobone and Sutanu Sarkar

Citation: *Physics of Fluids* (1994-present) **22**, 115108 (2010); doi: 10.1063/1.3505156

View online: <http://dx.doi.org/10.1063/1.3505156>

View Table of Contents: <http://scitation.aip.org/content/aip/journal/pof2/22/11?ver=pdfcov>

Published by the [AIP Publishing](#)

Articles you may be interested in

[Three-dimensionalization of the stratified mixing layer at high Reynolds number](#)

Phys. Fluids **23**, 111701 (2011); 10.1063/1.3651269

[Vertical mixing in homogeneous sheared stratified turbulence: A one-dimensional-turbulence study](#)

Phys. Fluids **23**, 055106 (2011); 10.1063/1.3592329

[Numerical investigation of the scalar probability density function distribution in neutral and stably stratified mixing layers](#)

Phys. Fluids **13**, 927 (2001); 10.1063/1.1352622

[Anisotropy of turbulence in stably stratified mixing layers](#)

Phys. Fluids **12**, 1343 (2000); 10.1063/1.870386

[Length scales of turbulence in stably stratified mixing layers](#)

Phys. Fluids **12**, 1327 (2000); 10.1063/1.870385



The statistical evolution of a stratified mixing layer with horizontal shear invoking feature extraction

Eric Arobone^{a)} and Sutanu Sarkar^{b)}

University of California-San Diego, 9500 Gilman Drive, La Jolla, California 92093-0411, USA

(Received 3 June 2010; accepted 17 September 2010; published online 11 November 2010)

Direct numerical simulations of a horizontally oriented shear layer are performed with various values of uniform vertical stratification. The effects of stratification on statistics such as turbulent Reynolds stress, turbulent kinetic energy, and viscous dissipation are examined. Comparisons between turbulent kinetic energy and scalar variance budgets among the unstratified and stratified cases are presented. In the stratified cases, spatially sparse coherent structures emerge, affecting transport of momentum and density. Additional physical insight gained from quantification of the influence of the coherent structures on the flow statistics such as turbulent scalar transport is summarized. Vortex ejection revealed vortical structure similar to that observed in prior investigations of the zigzag instability. © 2010 American Institute of Physics.

[doi:10.1063/1.3505156]

I. INTRODUCTION

Turbulent stratified flow with horizontal shear occurs in a wide variety of atmospheric and oceanographic scenarios. Boundary currents, wakes of towed or self-propelled objects, and flow from river deltas can all result in strong horizontal shear subjected to nearly vertical stratification. In geophysical flows, there is an abundance of horizontal kinetic energy organized into vortices whose vertical structure is of interest. While the effect of stratification on turbulent flow with vertical mean shear has received considerable attention in the case of two streams with uniform but different density¹⁻⁷ as well as in streams with ambient stratification,⁸⁻¹⁰ the horizontal case has only been investigated a handful of times.¹¹⁻¹³

The systematic study of flows with horizontal shear started with linear theory that was employed to study the effect of stratification on the stability of the mean flow profile. The instability of a two-dimensional shear flow, $U(x_2, x_3)$ with both vertical and horizontal shear in a medium with uniform buoyancy frequency, N , was investigated in Blumen¹⁴ under the assumptions of hydrostatic and inviscid perturbations. A sufficient condition for stability in the general situation of nonplanar shear was not found. In the simplified case of one-dimensional shear, $U(x_2)$, in a stratified fluid, instability was found to require an inflection point in the flow profile and developed an additional dependence on the vertical mode of oscillation. Three-dimensional instability of a horizontally oriented hyperbolic tangent mixing layer, $U(x_2) = U_0 \tanh(x_2/L)$ in a fluid with constant N was explored by Deloncle *et al.*¹⁵ because Squire's theorem does not apply to this particular flow. While the most unstable modes remain two-dimensional with (x_1, x_2) dependence, stratification was found to destabilize a broad range of three-dimensional perturbations. Three-dimensional perturbations

with $k_3 L < 1/Fr_h$, where $Fr_h = U_0/LN$ yielded growth rates very near those associated with two-dimensional perturbations.

Subsequently, nonlinear simulations into the regime of turbulence were carried out in the case of uniform shear flow. Linearized disturbances in flow with uniform shear do not show exponential growth but algebraic growth is possible. Nonlinearly evolving disturbances in unstratified flow with uniform shear develop into turbulence with exponentially growing kinetic energy. The case of uniform vertical mean shear, $U = Sx_3$ in a stratified fluid has been extensively studied and it is found that, for gradient Richardson number $Ri_g = N^2/S^2$ that exceeds a critical value (0.18–0.25), the turbulence is extinguished. The case of nonvertical shear was studied by Jacobitz and Sarkar¹¹ in a direct numerical simulation (DNS) study of stratified flow with mean velocity, $U = S \sin(\theta)x_2 + S \cos(\theta)x_3$. The case with purely horizontal shear, $\theta = \pi/2$, significantly showed higher turbulence levels compared to purely vertical shear. Nevertheless, for a sufficiently high stratification with $N^2/S^2 \approx 2$, the turbulence was extinguished in the case with purely horizontal shear as well.

The next step was a simulation of a turbulent flow with an inflectional mean velocity that develops linear instabilities. A shear layer with velocity difference ΔU in the horizontal (x_2) direction and uniform stratification was investigated by Basak and Sarkar,¹³ emphasizing the structure of the density and vorticity fields. Although the vertical velocity was suppressed by stratification, inflectional shear maintained horizontal velocity fluctuations preventing relaminarization. In the stratified cases, Kelvin–Helmholtz (KH) rollers merged to form coherent vortical structures that persisted for much longer times than in the unstratified case, where KH rollers were short-lived due to secondary instabilities. Corotating coherent structures also emerge in simulations of unstratified mixing layers at moderate Reynolds numbers,¹⁶ but buoyancy plays a greater role in dynamics than inhibiting vertical motion and affects the evolution of coherent struc-

^{a)}Electronic mail: earobone@ucsd.edu.

^{b)}Electronic mail: sarkar@ucsd.edu.

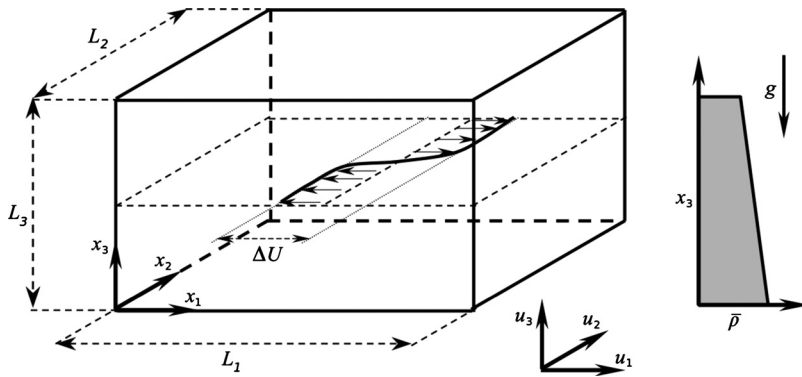


FIG. 1. Schematic of the mixing layer.

tures. A lattice of vortex cores, with vertical core height, l , such that $Fr = \Delta U / Nl = O(1)$, emerged in the stratified cases¹³ resulting from the tilting and truncation of columnar vortical structures. Density intrusions were found to laterally propagate from the shear layer owing to buoyant parcels of fluid expelled from the coherent structures laterally spreading much like gravity currents.

Given the occurrence of coherent vortices with vertical structure in the simulations¹³ of *turbulent* flow with horizontal shear, it is appropriate to review the literature on vertical structure of stratified vortices in simpler configurations. A pair of counter-rotating vortices was experimentally shown by Billant and Chomaz¹⁷ to undergo a zigzag instability characterized by a vertically modulated twisting and bending of the vortex pair. The accompanying theoretical analysis¹⁸ suggests that the vertical wavelength l_3 corresponds to $Fr = u_h / Nl_3 \sim O(1)$. Waite and Smolarkiewicz¹⁹ performed simulations of a stratified counter-rotating vortex pair at a Reynolds number higher than explored in the laboratory experiment. The early time evolution agreed with linear analysis and experiments of the zigzag instability^{17,18} while the late-time evolution was qualitatively different owing to transition to turbulence. Deloncle *et al.*²⁰ performed DNS of the zigzag instability, similar to Waite and Smolarkiewicz, and showed that the transition to turbulence occurs at large buoyancy Reynolds number. The instability of a tilted Oseen–Lamb vortex was experimentally investigated by Boulanger *et al.*²¹ for the case of small inclination angles. Thin strips along the edge of the vortices showed strong shear and large density variation. Along the edges of the vortex, shear layer and jet instabilities are observed. This instability was observed at higher Froude numbers than the zigzag instability.

The current work, in contrast to the previous study of a horizontally oriented shear layer,¹³ focuses on the evolution of flow statistics in the shear layer including examination of the role of coherent structures. Quantitative assessment of the role of coherent structures requires means to isolate coherent vortical flow from the rest of the flow field. Since a universally accepted definition of a vortex is currently unavailable, multiple methods of feature extraction were considered. Several commonly used vortex eduction criteria using information contained in the rate of deformation tensor, $\nabla \mathbf{u}$, are introduced in Chong *et al.*²² and Jeong and Hussain,²³ and assessed in Chakraborty *et al.*²⁴ and Haller.²⁵ For example, the Q criterion defines a vortex as a region

where the norm of the rate of rotation tensor, $\|\boldsymbol{\Omega}\|$, exceeds the norm of the rate of strain tensor, $\|\mathbf{S}\|$. The Δ criterion defines vortices as the regions of flow where $\nabla \mathbf{u}$ has complex eigenvalues, implying locally swirling flow. λ_2 identifies vortices as regions of the flow where the rotational rate exceeds strain rate only in a specific plane. Coherent vortex extraction²⁶ separates an incoherent (small-amplitude) component from a given field. Since wavelets are isolated both with respect to length scale and physical location, they are especially suitable for stratified flows that are dominated by sparse multiscale features. This motivates an examination of wavelet-based decomposition of the vorticity field in the present problem.

II. PROBLEM DEFINITION

A temporally evolving shear layer representing two streams with velocity difference ΔU is subjected to uniform stable stratification in the vertical direction. The streamwise velocity (u_1) only varies in the transverse (x_2) direction, where the initial vorticity thickness ($\delta_{\omega,0}$) characterizes the width of the region separating the streams. The streamwise (x_1) and vertical (x_3) directions are assumed to be infinite and homogeneous. Kinematic viscosity and thermal diffusion are denoted by ν and κ , respectively. Figure 1 shows a detailed schematic.

A. Initial conditions

The initial mean flow field is given by a hyperbolic tangent velocity profile of the following form:

$$\langle u_1 \rangle = \frac{\Delta U}{2} \tanh\left(\frac{2x_2}{\delta_{\omega,0}}\right), \quad \langle u_2 \rangle = 0, \quad \langle u_3 \rangle = 0. \quad (1)$$

Flow variables are decomposed into mean and fluctuation quantities via the Reynolds decomposition. Averaging is performed in the homogeneous directions, x_1 and x_3 . Quantities surrounded by angle brackets represent means and primed variables represent fluctuations. The vorticity thickness of the mixing layer is given by

$$\delta_{\omega} = \frac{\Delta U}{\max\{\partial \langle u_1 \rangle / \partial x_2\}}. \quad (2)$$

The initial fluctuating field is prescribed with three-dimensional fluctuations having an energy spectrum, $E(k)$

TABLE I. Boundary conditions at the transverse boundaries.

$u_1(x_1, -L_2/2, x_3) = -0.5$	$u_1(x_1, L_2/2, x_3) = 0.5$
$u_2(x_1, -L_2/2, x_3) = 0$	$u_2(x_1, L_2/2, x_3) = 0$
$u_3(x_1, -L_2/2, x_3) = 0$	$u_3(x_1, L_2/2, x_3) = 0$
$\rho'(x_1, -L_2/2, x_3) = 0$	$\rho'(x_1, L_2/2, x_3) = 0$
$p'(x_1, -L_2/2, x_3) = 0$	$p'(x_1, L_2/2, x_3) = 0$

$= Ck^4 e^{-2(k/k_0)^2}$, which accelerates transition to turbulence. The peak wavenumber, k_0 , is selected to correspond with a wavelength of $1.7\delta_{\omega,0}$. The initial turbulent kinetic energy is $K_0(x_2) = 0.029(\Delta U)^2 \exp[-(x_2/\delta_{\omega,0})^2]$, such that fluctuation energy peaks at the midplane of the shear layer.

B. Governing equations

The dimensional equations for conservation of mass, momentum, and density of an incompressible fluid are given below (dimensional variables indicated by *)

$$\text{continuity: } \frac{\partial u_i^*}{\partial x_i^*} = 0, \quad (3)$$

$$\text{momentum: } \frac{\partial u_i^*}{\partial t^*} + \frac{\partial(u_i^* u_j^*)}{\partial x_j^*} = -\frac{1}{\rho} \frac{\partial p^*}{\partial x_i^*} + \nu \frac{\partial^2 u_i^*}{\partial x_j^* \partial x_j^*} - g \delta_{i3}, \quad (4)$$

$$\text{density: } \frac{\partial \rho^*}{\partial t^*} + \frac{\partial(\rho^* u_j^*)}{\partial x_j^*} = \kappa \frac{\partial^2 \rho^*}{\partial x_j^* \partial x_j^*}. \quad (5)$$

The density and pressure fields are decomposed in the following manner:

$$\rho^*(x_i, t) = \rho_0 + \bar{\rho}(x_3) + \rho'^*(x_i, t), \quad (6)$$

$$p^*(x_i, t) = \bar{p}(x_3) + p'^*(x_i, t), \quad (7)$$

where $\bar{\rho}(x_3)$ represents the background stratification and $\bar{p}(x_3)$ represents hydrostatic pressure balancing the initial density profile ($\rho_0^* = \rho_0 + \bar{\rho}$). The nondimensional variables for this problem are given as

$$t = \frac{t^* \Delta U}{\delta_{\omega,0}}, \quad x_i = \frac{x_i^*}{\delta_{\omega,0}}, \quad u_i = \frac{u_i^*}{\Delta U}, \quad (8)$$

$$\rho' = \frac{-\rho'^*}{\delta_{\omega,0}(d\bar{\rho}/dx_3)}, \quad p' = \frac{p'^*}{\rho_0 \Delta U^2}. \quad (9)$$

TABLE II. Simulation parameters.

Case	Re_0	$Ri_{b,0}$	Pr	L_1	L_2	L_3	N_1	N_2	N_3
A0	680	0	1	43.0	25.8	12.9	640	384	192
A1	680	0.113	1	86.0	68.8	25.8	640	512	192
A2	680	0.358	1	86.0	68.8	25.8	640	512	192
A3	680	1.132	1	86.0	68.8	25.8	640	512	192
A3 _{low}	680	1.132	1	86.0	68.8	25.8	640	512	192
2D	680	...	1	3440	51.6	0	25 600	384	1

When Boussinesq approximations are assumed, the following nondimensional equations are obtained:

$$\text{continuity: } \frac{\partial u_i}{\partial x_i} = 0, \quad (10)$$

$$\text{momentum: } \frac{\partial u_i}{\partial t} + \frac{\partial(u_i u_j)}{\partial x_j} = -\frac{\partial p'}{\partial x_i} + \frac{1}{Re_0} \frac{\partial^2 u_i}{\partial x_j \partial x_j} - Ri_{b,0} \rho' \delta_{i3}, \quad (11)$$

$$\text{density: } \frac{\partial \rho'}{\partial t} + \frac{\partial(\rho' u_j)}{\partial x_j} - u_j \delta_{j3} = \frac{1}{Re_0 Pr} \frac{\partial^2 \rho'}{\partial x_j \partial x_j}, \quad (12)$$

where

$$Re_0 = \frac{\Delta U \delta_{\omega,0}}{\nu}, \quad Ri_{b,0} = -\frac{g}{\rho_0} \frac{d\bar{\rho}}{dx_3} \frac{\delta_{\omega,0}^2}{\Delta U^2} = \frac{N^2 \delta_{\omega,0}^2}{\Delta U^2},$$

$$Pr = \frac{\nu}{\kappa}.$$

Here, Pr is taken to be unity for the sake of reasonable computational cost. Dirichlet boundary conditions are enforced for all flow variables at the transverse boundaries where flow variables are fixed to the values given in Table I. Periodicity is enforced in the streamwise and vertical directions through Fourier decomposition. Boundary influence increases with time as the shear layer grows.

C. Computational method

The numerical algorithm is different from Basak and Sarkar¹³ who employed a second-order finite difference method in all directions. Instead, we employ spectral collocation in the streamwise and vertical directions and second-order finite difference in the transverse direction. The transverse velocity is stored on a grid staggered in the transverse direction. The Navier–Stokes and density equations are marched using a third order mixed Runge–Kutta/Crank–Nicolson time scheme with viscous terms implicitly treated. A Rayleigh damping function is used near the $x_2 = \pm L_2/2$ boundaries, with a width of approximately $3\delta_{\omega,0}$, to prevent spurious reflections. The Poisson equations for pressure and removal of velocity divergence are solved using the Thomas algorithm. Parallelization is accomplished using Message Passing Interface. Case specific computational details are shown in Table II.

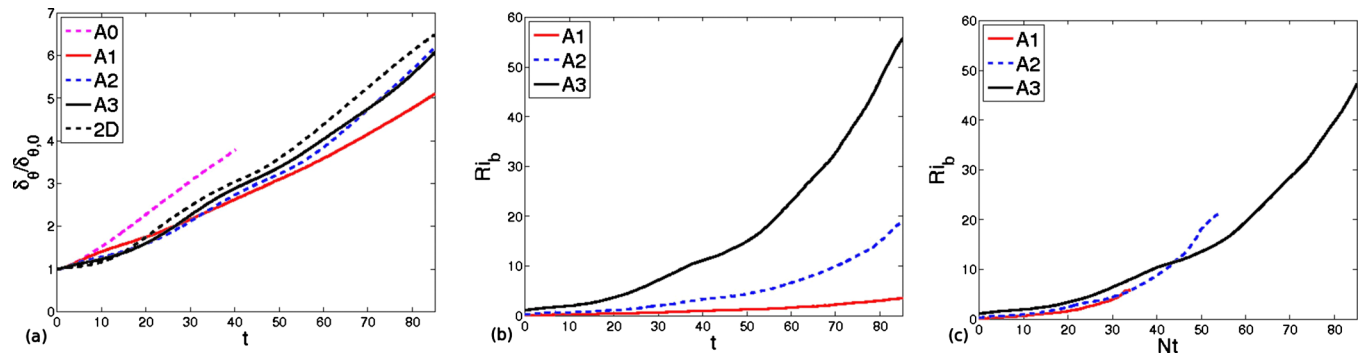


FIG. 2. (Color online) (a) The evolution of momentum thickness of the shear layer. The evolution of bulk Richardson number as a function of (b) t and (c) Nt . To convert from t to Nt multiply by 0.336, 0.828, and 1.064 in stratified cases A1, A2, and A3, respectively.

D. Case study

Six simulations were performed as listed in Table II, five of which used the initial conditions described in Sec. II A. Case A0 investigates the evolution of an unstratified mixing layer, while cases A1, A2, and A3 explore the effect of various values of uniform stratification. For comparison, case 2D investigates the evolution of a two-dimensional mixing layer. Case A3_{low} is identical to case A3, however, initial velocity fluctuations have an amplitude smaller by a factor of 10^{-3} . This allows investigation of the effect of linearly evolving initial conditions on statistical evolution and the formation of vortical structures. In case 2D, a very large value of L_1 was used so that statistics would be reproducible, since averaging is performed across pencils instead of planes as in the 3D simulations.

III. EFFECTS OF BUOYANCY ON MEAN FLOW AND TURBULENT STRESSES

The bulk Richardson number ($Ri_b = N^2 \delta_\omega^2(t) / \Delta U^2$) represents the ratio of the stabilizing effect of buoyancy to the destabilizing effect of horizontal shear. N^2 is varied between simulations to investigate the effect of stratification on dynamics. In addition to an unstratified case, a two-dimensional simulation was performed for comparison against the limit of $N^2/S^2 \gg 1$. Statistics from case A0 validated well against the

results of Pantano and Sarkar²⁷ and Basak and Sarkar.¹³ Thickness growth rates, $Ri_b(Nt)$, and visualizations of vorticity components agreed well with the results of Basak and Sarkar¹³ for stratified runs. Growth rates for the two-dimensional and stratified cases are shown in Fig. 2(a). Here, growth rate is defined using the momentum thickness,

$$\delta_\theta = \int_{-L_2/2}^{L_2/2} \frac{1}{4} - \left(\frac{\langle u_1 \rangle(x_2)}{\Delta U} \right)^2 dx_2.$$

Plots of $Ri_b(Nt)$ and $Ri_b(t)$ for the stratified simulations are given in Figs. 2(b) and 2(c). $Ri_b(Nt)$ is nearly proportional to $(Nt)^2$, implying the eventual dominance of stratification effects in all stratified cases. In case A3, the bulk Richardson number reached values in excess of 80, while exhibiting substantial vertical variability.

A. Self-similarity of turbulence statistics and the $Ri_b \gg 1$ limit

The temporal evolution of turbulence intensities in cases with high stratification, (A3 and A2) show an approach to an asymptotic profile, indicative of self-similar evolution. Figure 3(a) illustrates the evolution toward self-similarity in profiles of the spanwise root mean square fluctuations for case A3. After an initial transient, turbulence levels in stratified cases primarily depend on the local value of $Ri_b(t)$. This

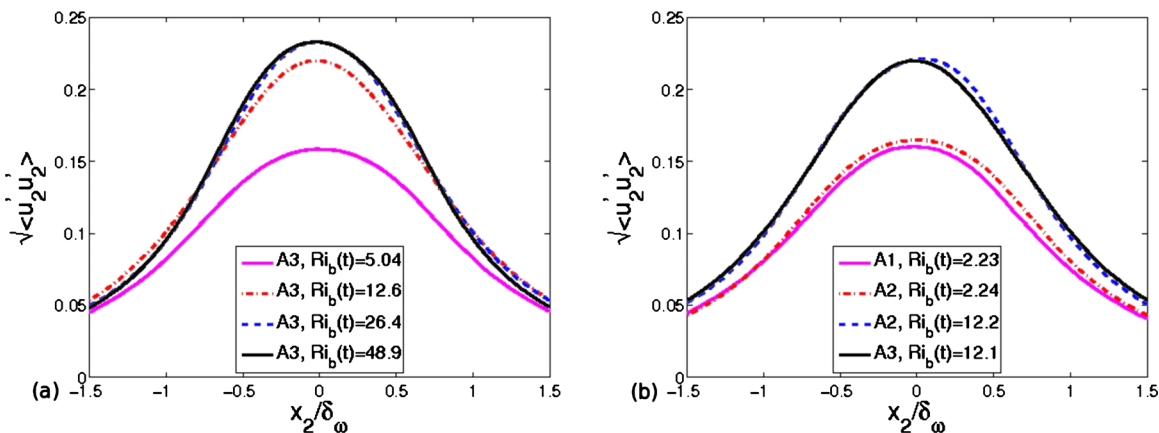


FIG. 3. (Color online) Profiles of transverse fluctuations. (a) Evolution in the strongly stratified case (A3). (b) Cases A1 and A2 at different times but matching Ri_b . Similarly, cases A2 and A3 at different times but matching Ri_b .

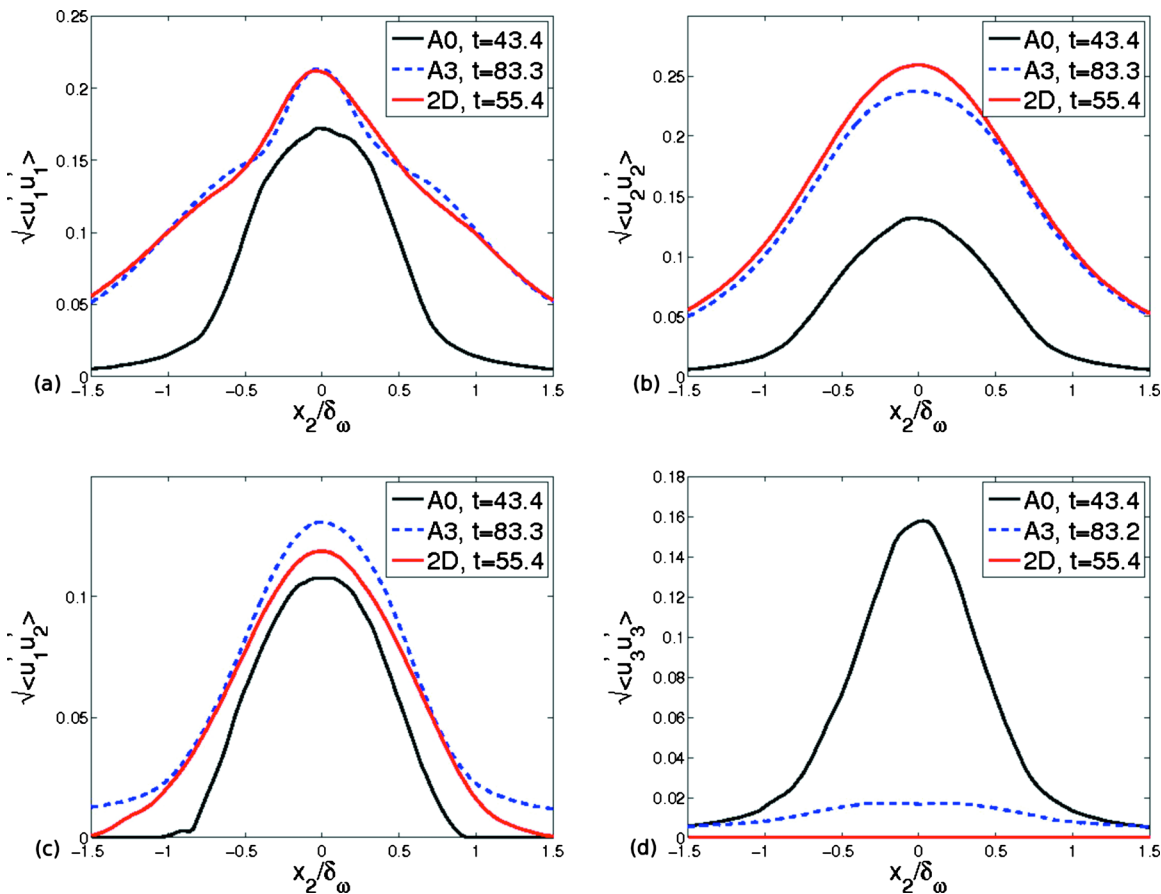


FIG. 4. (Color online) Comparison of self-similar statistics of stratified, unstratified, and two-dimensional simulations.

result is illustrated by Fig. 3(b) that compares profiles between the stratified cases at comparable values of $Ri_b(t)$. The A0 case also reaches self-similar energetic profiles after a much shorter initial transient process due to its intense turbulent fluxes. Additionally, the 2D case reaches self-similar behavior far more quickly than the stratified cases.

In the limit of $Ri_b(t) \gg 1$, turbulence statistics such as $\langle u_1' u_1' \rangle$, $\langle u_2' u_2' \rangle$, $\langle u_1' u_2' \rangle$, and $\langle \rho' u_3' \rangle$ lose their dependence on $Ri_b(t)$ in the stratified simulations and, therefore, self-similar evolution is observed. Case A3 exhibits self-similar energetics over the longest range of time while case A2 briefly exhibits self-similarity before experiencing strong boundary effects. Nevertheless, because $Ri_b \propto (Nt)^2$, eventually all flows with nonzero N will reach the $Ri_b \gg 1$ limit as suggested in Fig. 2(c).

The influence of initial disturbance levels was also explored for the stratification present in case A3. Most second-order turbulence statistics showed agreement between cases A3 and A3_{low} after an initial adjustment period. Other statistics, such as $\langle u_3' u_3' \rangle$ and $\langle \rho' \rho' \rangle$, showed some differences dependent upon the initial turbulent kinetic energy.

According to Billant and Chomaz²⁸ for a strongly stratified inviscid flow with quasihorizontal eddies that self-similarly evolves vertical velocity fluctuations should scale such as $u_3' \sim \Delta U Ri_b^{-1/2}$ and scalar fluctuations should scale such as $\rho' \sim (d\bar{\rho}/dx_3)\delta_\omega Ri_b^{1/2}$. For cases A1 and A2 this type

of scaling does not seem to hold in the self-similar regime. Case A3 however appears to have a small enough horizontal Froude number for the strongly stratified assumption to hold and a similar scaling is observed.

B. Comparisons among unstratified, stratified, and two-dimensional results

Comparisons are made among the statistics of unstratified, stratified, and two-dimensional shear layers once self-similarity is attained. The stratified cases show the emergence of coherent vortical structures as illustrated later in Fig. 10. These coherent structures change turbulence profiles as discussed below.

Statistical quantities of interest are presented in Fig. 4, showing key similarities and differences. Profiles of $\langle u_1' u_1' \rangle$ and $\langle u_2' u_2' \rangle$ in the stratified cases are very similar to those found in the two-dimensional shear layer. The agreement is due to the coherent nature of the ω_3 field associated with the columnar coherent structures. Turbulent shear stress $\langle u_1' u_2' \rangle$ shows reasonable agreement between the two-dimensional and stratified cases except outside of $|x_2| < \delta_\omega$ where for the stratified case, shear stress takes much larger values than the two-dimensional case. This is due to the formation of density intrusions that laterally propagate from the shear region. These intrusions advect slower-than-ambient flow in the

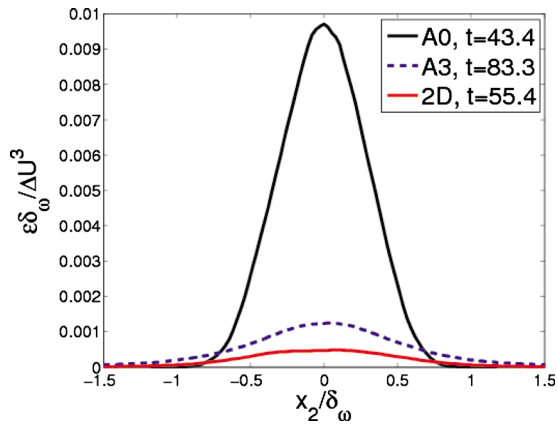


FIG. 5. (Color online) Comparison of dissipation from stratified, unstratified, and two-dimensional simulations.

transverse direction, contributing to the increased levels of $\langle u'_1 u'_2 \rangle$ well outside of the region containing vortical structures.

The profile of $\langle u'_1 u'_1 \rangle$ in cases A3 and 2D, Fig. 4(a), develops a profile consisting of two distinct regions. The region close to the centerline ($|x_2| < \delta_\omega/2$), we designate the “head” of the profile while the surrounding region we identify as the “shoulders.” The development of the head coincides with vortex staggering, which would not emerge if vortices were centered about the centerline. In fact, for a row of Rankine vortices $\langle u'_1 u'_1 \rangle$ would take the value of zero at the centerline. The centerline value of transverse fluctuations $\langle u'_2 u'_2 \rangle$ show significant growth in the stratified runs due to coherent structures with well organized ω_3 fields, increasing transverse momentum transfer in comparison to the weakly organized vorticity field observed in case A0.

IV. EVOLUTION OF DISSIPATION STATISTICS

Irreversible viscous dissipation of fluctuating kinetic energy, ϵ , is defined as $\epsilon = (2/Re_0) \langle s'_{ij} s'_{ij} \rangle$, where $s'_{ij} = 1/2(u'_{i,j} + u'_{j,i})$. Irreversible dissipation of scalar variance due to diffusive effects, ϵ_ρ , is defined as $\epsilon_\rho = (2/Re_0 Pr) \langle \rho'_i \rho'_i \rangle$.

A substantial reduction in turbulent dissipation is observed in the presence of stratification, as shown in Fig. 5. Dissipation, however, does not decrease to the levels found in two-dimensional simulations due to the large vertical gra-

dients of velocity induced by buoyancy. Turbulent dissipation maintains integrated values ($\int_{-L_2/2}^{L_2/2} \epsilon dx_2$) at least two to three times larger in the stratified cases than observed in the two-dimensional case. Thin dislocations of vorticity develop as vertical shearing leads to pockets of vorticity subjected to strong vertical viscous diffusion greatly contributing to energy dissipation. The vertical distance across these dislocations, i.e., the dislocation thickness is small compared to horizontal thickness.

Time evolution of the integrated fluctuating viscous and scalar dissipations as well as buoyancy Reynolds number, $Re_B = \epsilon / \nu N^2$, are plotted for the stratified cases in Fig. 6. The reproducible results of self-similarity seen in the evolution of turbulent stresses do not apply to turbulent and scalar dissipation until much later in the simulations. These show significant variation between cases A1 and A3, which is likely due to the differences in dislocation thickness. Dislocation thickness, l_d scales with $\sqrt{\nu/N}$ between cases that helps explains why the integrated dissipation reaches its largest values in case A3. Case A1 shows higher values of integrated dissipation initially due to the far greater presence of small scale turbulence, but vertical gradients become so significant in the dislocations that case A3 eventually dominates.

Initially, there is a drop in viscous dissipation, seen in Fig. 6(a), as viscosity suppresses high wavenumber components of the initial fluctuations. The subsequent drop in dissipation when $5 \leq t \leq 20$ corresponds to the time when the vorticity field organizes into large columnar vortices. It is plausible that the 2D curve could represent the limit of $N^2/S^2 \rightarrow \infty$ during this process. The following period over which dissipation increases, $20 \leq t \leq 80$, is when dislocations form and grow as a result of vertical shearing and instabilities acting on the vortices. The slope at which dissipation increases during this time period is proportional to N in the stratified cases, implying that buoyancy plays a role in the small scale dynamics of these cases.

The buoyancy Reynolds number shows a steep decrease initially in case A1 that continues until boundary effects become significant. The increase in dissipation due to dislocations is so significant in case A3 that the centerline value of ϵ increases when $40 \leq Nt \leq 80$. This intensification of centerline dissipation could result in a reemergence of turbulent behavior at late time, provided dislocations contain suffi-

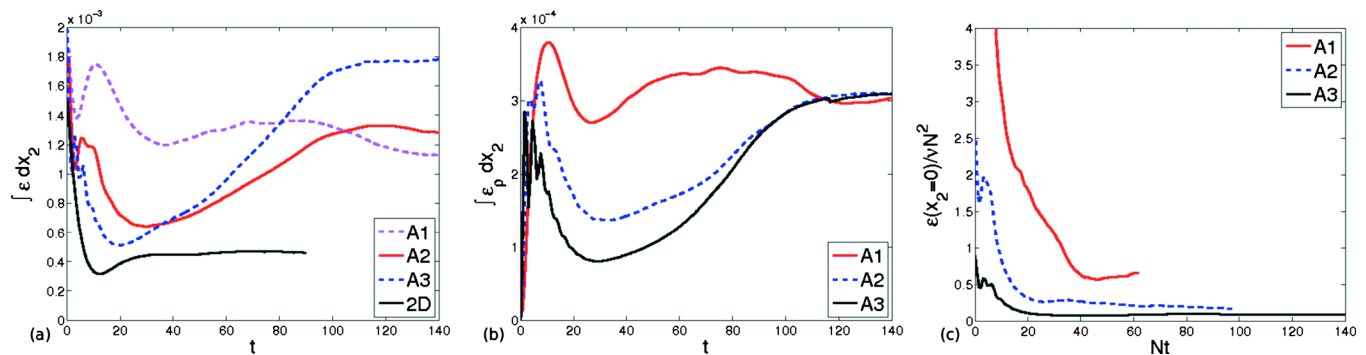


FIG. 6. (Color online) Evolution of (a) integrated viscous dissipation, (b) integrated scalar dissipation, and (c) the buoyancy Reynolds number, $Re_B = \epsilon / \nu N^2$ at the x_2 midplane.

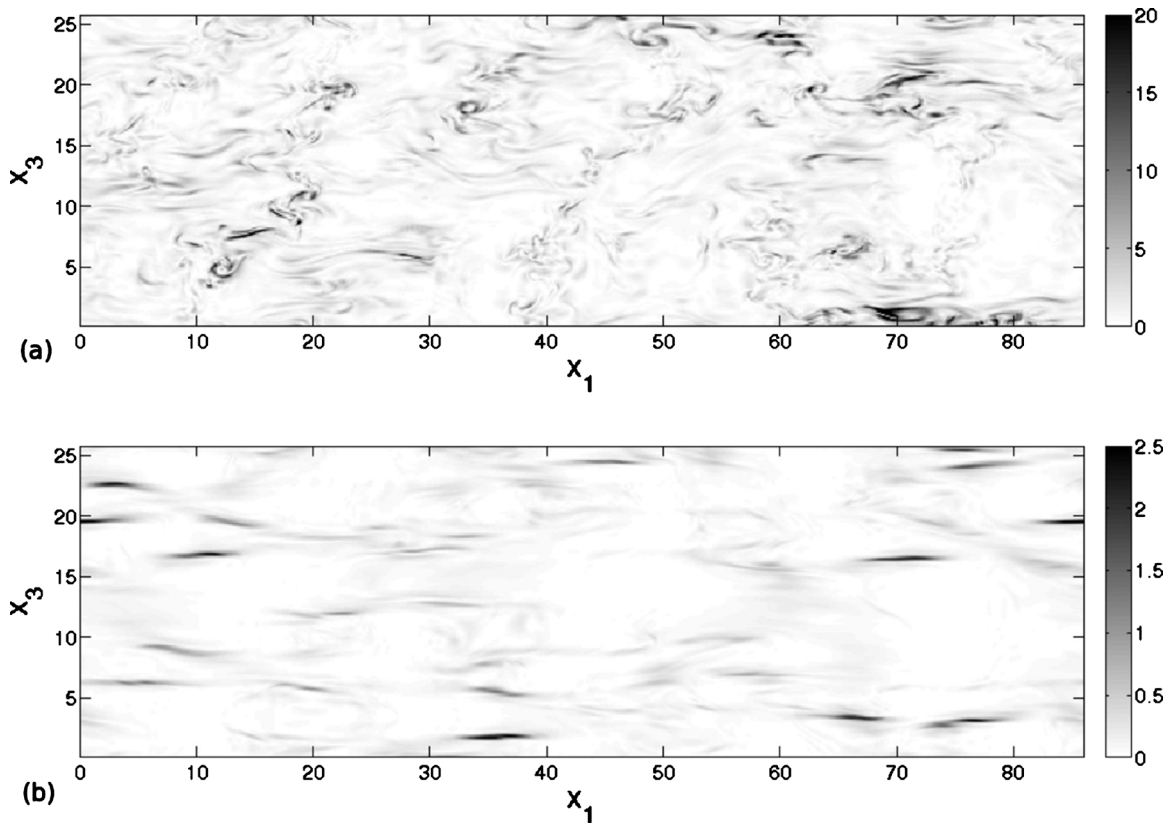


FIG. 7. Vertical cuts of the x_2 midplane with $\tilde{\epsilon}/\nu N^2$ from (a) the weakly stratified case (A1) and (b) the strongly stratified case (A3) (bottom) at times $t=84.2$ and $t=82.2$, respectively.

ciently strong vertical shear for Kelvin–Helmholtz instabilities and turbulence to overcome stratification.

Slices of local $\widetilde{\text{Re}}_B = \tilde{\epsilon}/\nu N^2$ are shown in the x_2 midplane for cases A1 and A3 in Fig. 7. In both cases, localized patches of high $\widetilde{\text{Re}}_B$ are seen, which explains why turbulent behavior is observed in case A1, although the mean value is $\text{Re}_B \approx 1.28$. In all three stratified cases, the ratio of $\epsilon_{\text{max}}/\tilde{\epsilon}$ takes values between 30 and 50 due to the localized nature of the dissipation field after the formation of spatially sparse dislocations. Thus, although the mean buoyancy Reynolds number is close to unity, the flow is far from laminar. The dissipation is also highly anisotropic, i.e., the contribution of vertical gradients of horizontal velocity dominate at large Ri_b . The values of Re_B in all three stratified cases are much smaller than those observed in the ocean (e.g., Equatorial Undercurrent system), which is due to both physics and computational limitations. The lack of baroclinicity and mean vertical shear keeps dissipation relatively small and isolated. Additionally, since DNS is used Re_0 takes values much smaller than expected for a typical horizontal shear flow in the ocean, which indirectly tends to reduce Re_B values.

Local gradient Richardson numbers $\text{Ri}_g = N^2/(u_{1,3}^2 + u_{2,3}^2)$ of order one are common within the coherent structures. This result is consistent with the hypothesis of Lilly²⁹ and results of Riley and de Bruyn Kops.³⁰ Vertical shear is intense within the dislocations leading to local Richardson numbers of less than a half in case A3. Visualizations of local Ri_g are

nearly identical to local Re_B , especially in case A3, and hence not included.

V. TURBULENT KINETIC ENERGY BUDGETS

The evolution equation for the fluctuating kinetic energy is

$$\frac{\partial K}{\partial t} = P - \epsilon + B - \frac{\partial T}{\partial x_2}. \quad (13)$$

Here, K represents turbulent kinetic energy (TKE) defined as

$$K = \frac{1}{2} \langle u'_i u'_i \rangle, \quad (14)$$

P represents shear-generated production of turbulent kinetic energy defined as

$$P = - \langle u'_1 u'_2 \rangle \frac{\partial \langle u_1 \rangle}{\partial x_2}, \quad (15)$$

B represents the buoyancy flux or rate of exchange between turbulent kinetic and potential energies defined as

$$B = - \text{Ri}_{b,0} \langle \rho' u'_3 \rangle, \quad (16)$$

and T represents the transport of turbulent kinetic energy through turbulent motions (T_t), pressure correlations (T_p), and viscous diffusion (T_v) defined as

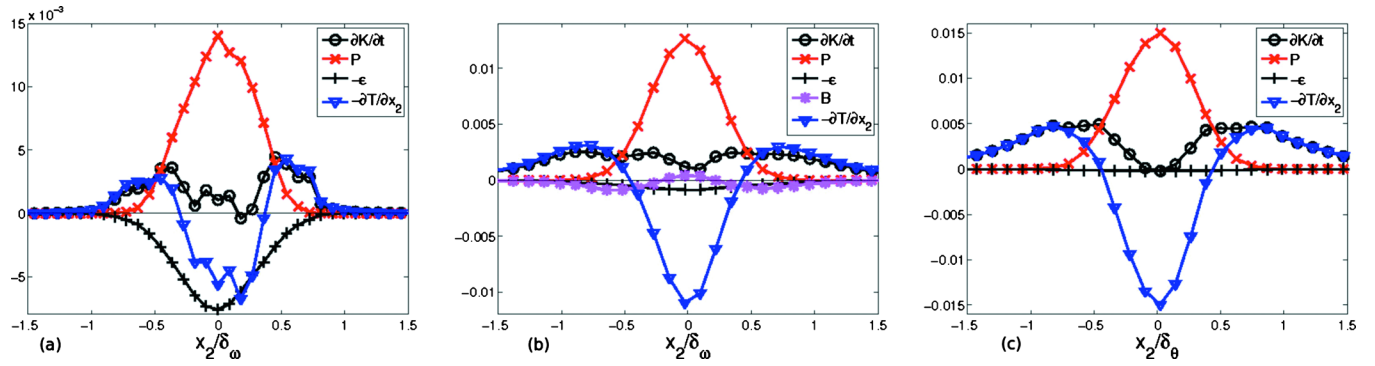


FIG. 8. (Color online) Turbulent kinetic energy budgets for (a) the unstratified case (A0) at time $t=21.29$, (b) the strongly stratified case (A3) at time $t=70.66$, and (c) 2D at time $t=66.31$. The terms have been normalized with $\Delta U^3/\delta_\omega(t)$.

$$T = T_t + T_p + T_v, \quad (17)$$

$$= \frac{1}{2} \langle u'_i u'_i u'_2 \rangle + \langle p' u'_2 \rangle - \frac{2}{\text{Re}_0} \langle u'_i s'_{i2} \rangle. \quad (18)$$

The TKE budgets for the cases A0, A3, and 2D are presented in Figs. 8(a)–8(c), respectively. In the unstratified (A0) budget the production, transport, and dissipation are all significant. Away from the centerline, turbulent production and transport exceed dissipation leading to TKE generation, while at the centerline there is an approximate balance. In the stratified (A3) budget the dominant balance is between production and transport; the dissipation and buoyancy flux have smaller values. The magnitude of integrated dissipation considerably varies between stratified cases, but the relatively small influence of dissipation on the energy budget helps explain why energetics, such as $\langle u'_i u'_i \rangle$ do not vary between cases for sufficiently large Ri_b even though dissipation does vary. Lateral transport is significantly more effective in the stratified cases than case A0, owing to the well organized ω_3 field associated with the coherent structures. The dominant balance of the two-dimensional (2D) budget is also between turbulent production and turbulent transport with production and transport varying very similarly to A3 with respect to x_2/δ_ω . Dissipation plays an even less significant role in the 2D budget as expected from the results in Sec. IV.

The buoyancy flux is a relatively small term in the energy budget at late time. Shear instabilities in the mean flow do not directly contribute to the formation of $\omega_h = \sqrt{\omega_1^2 + \omega_2^2}$, which can only be generated through secondary instabilities. Buoyancy flux is positive at the centerline, where vortical structures tend to tilt away from the vertical due to baroclinic torque, resulting in an exchange from potential to kinetic energy. The lattice of tilted vortical structures advects fluid away from their equilibrium position as ambient flow is entrained, resulting in negative buoyancy flux away from the centerline.

While internal waves are present outside of the coherent structures in the stratified cases, their amplitudes are small and they transport little energy away from the shear layer. In case A3, the energy flux $\langle p' u'_2 \rangle$ very similarly evolves to the internal wave free 2D case.

VI. SCALAR VARIANCE BUDGETS

The evolution of scalar variance is examined to understand scalar transport and mixing. The evolution equation for scalar variance is

$$\frac{\partial \langle \rho' \rho' \rangle}{\partial t} = P_\rho - \epsilon_\rho - \frac{\partial T_\rho}{\partial x_2}. \quad (19)$$

Since N^2 is uniform throughout the domain, turbulent potential energy, K_ρ , is directly proportional to scalar variance and has the following evolution equation:

$$\frac{\partial K_\rho}{\partial t} = \frac{\text{Ri}_b}{2} \left(P_\rho - \epsilon_\rho - \frac{\partial T_\rho}{\partial x_2} \right). \quad (20)$$

Here, P_ρ is the nondimensional production of scalar variance due to motion in the vertical direction defined as

$$P_\rho = 2 \langle \rho' u'_3 \rangle. \quad (21)$$

Note that the dimensional production given by $-2 \langle \rho^{*'} u_3^{*'} \rangle d \langle \rho^{*'} \rangle / dx_3^*$ takes the above form owing to the non-dimensionalization used here. The term T_ρ or scalar transport, which is split into turbulent scalar transport ($T_{\rho,t}$) and viscous scalar transport ($T_{\rho,v}$), is defined as

$$T_\rho = T_{\rho,t} + T_{\rho,v}, \quad (22)$$

$$= \langle \rho' \rho' u'_2 \rangle - \frac{2}{\text{Re}_0 \text{Pr}} \frac{\partial \langle \rho' \rho' \rangle}{\partial x_2}. \quad (23)$$

It should be noted that for the unstratified budget we assume that the flow is actually vertically stratified, but density acts as a passive scalar since the buoyancy term is neglected for $\text{Ri}_b=0$. This is equivalent to investigating a stratified fluid in the absence of a gravitational field.

Figures 9(a) and 9(b) show distinct differences between the stratified and unstratified budgets. Greater lateral spread of profiles in the stratified cases is consistent with previous results, such as the profiles in Fig. 3. While the terms in the unstratified budget tend to subside where $|x_2| \gtrsim \frac{1}{2} \delta_\omega$, the terms from the stratified cases do not tend to zero until $|x_2| \gtrsim \delta_\omega$ indicating that shear induced scalar stirring and mixing occur over significantly larger horizontal length scales.

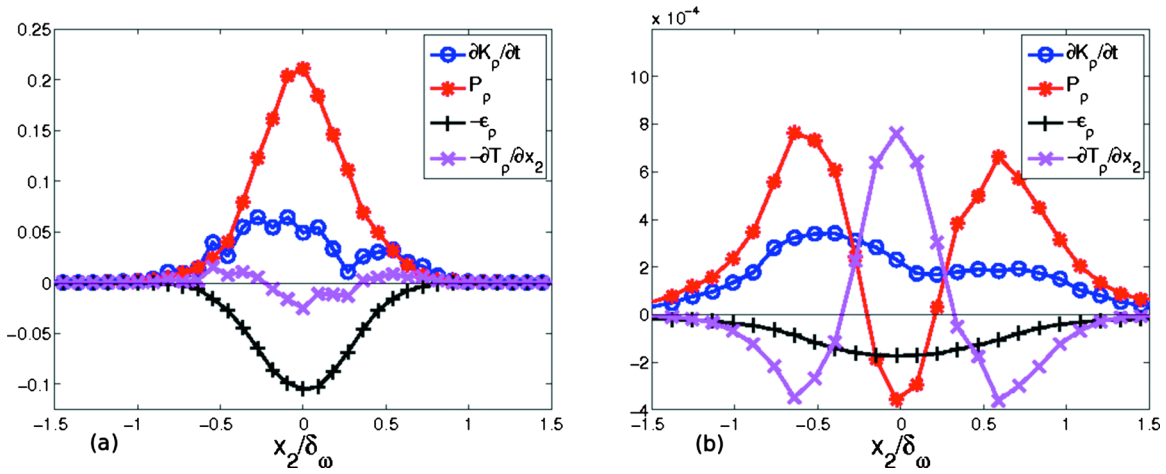


FIG. 9. (Color online) Scalar variance budgets for (a) the unstratified case (A0) at time $t=21.29$ and (b) the strongly stratified case (A3) at time $t=70.66$. Each term is normalized with $(d\bar{p}/dz)^2\Delta U\delta_\omega(t)$.

The distinct differences between the two budgets are also observed in the production and turbulent transport terms. In the unstratified case a relatively small down-gradient transport is present as in Fig. 9(a), while in the stratified case larger countergradient transport is observed in Fig. 9(b). The difference in relative magnitudes of the transport terms between the budgets is a direct result of more effective lateral transport when coherent structures are present. Additionally, while density variance is produced near the centerline in the passive scalar case, one observes density variance destruction near the centerline and production outside of the vortical structures in the stratified cases.

The behavior of the production term, P_ρ , in the scalar variance budget for case A3 can be explained as follows. The positive value of P_ρ at the flanks of the shear layer can be understood from the following argument inspired by previous investigation of a tilted columnar vortex.²¹ In the stratified cases, large quasivertical coherent structures emerge with tilt in both the stream-wise and transverse directions resulting in small vertical velocities concentrated at the edges of the vortices. As flow is entrained from the ambient it tends to be displaced from its equilibrium position resulting in large positive P_ρ away from the structures. The negative value of P_ρ in the central region of the shear layer occurs because the fluid that has been stirred up at the peripheries and transported into the central region cannot be maintained out of static equilibrium by the suppressed vertical velocity. Thus P_ρ acts to transfer energy from potential to kinetic modes during the return of fluid parcels to their equilibrium position.

VII. ROLE OF COHERENT STRUCTURES

A. Identification

The method of feature extraction utilized in the current study is the λ_2 criterion, due to minimal presence of noise, clear physical interpretation, and ability to better isolate vortex cores and braid regions compared to both Q and Δ . λ_2 is considered a strong vortex identification scheme in the case of incompressible nonrotating systems.^{24,25} It is de-

finied as the median eigenvalue of the symmetric tensor $S_{ik}S_{kj} + \Omega_{ik}\Omega_{kj}$, where Ω_{ij} and S_{ij} represent the rate of strain and rate of rotation tensors defined as $S_{ij} = \frac{1}{2}(u_{i,j} + u_{j,i})$ and $\Omega_{ij} = \frac{1}{2}(u_{i,j} - u_{j,i})$, respectively.

B. Evolution of coherent structures

Figure 10 shows several snapshots of λ_2 isosurfaces to illustrate the evolution of coherent structures in the mixing layer. In Fig. 10(a), at $t=0$, the field is incoherent because of the initial high wavenumber fluctuations, but stratification quickly suppresses ω_h and quasivertical structures emerge as in Fig. 10(b). These structures experience strong vertical shear ($\partial u_2/\partial x_3$) due to buoyancy induced effects reminiscent of the zigzag instability. The vertical shear distorts vortical structures causing them to dislocate and then separate leading to the formation of a field of dislocated vortex cores.

C. Zigzag instability

Experiments performed by Billant and Chomaz¹⁷ of a vertically oriented pair of counter-rotating columnar vortices in the presence of various levels of vertical stratification show the formation of the zigzag instability, which behaves differently from the elliptical instability commonly observed in the absence of stratification.³¹ An instability similar to the zigzag instability was also observed in the stratified simulations, e.g., case A3, shown in Fig. 11(a). This slicing plays an important role in introducing vertical variability and vertical gradients into the flow field, by shearing apart columnar vortical structures.

The zigzaglike slicing causes the transition of columnar vortices to pancake vortices by tilting segments of the vortices in the transverse direction. The segments of the vortices that have been displaced in the transverse direction then are advected downstream by the mean flow shearing apart the vortices until pancake vortices form. The vertical length scale associated with the instability, l_3 similarly corresponds to the length scales associated with $Fr \sim O(1)$, as in prior observations of the zigzag instability.^{17,19}

A simulation was performed of a single quasivertically

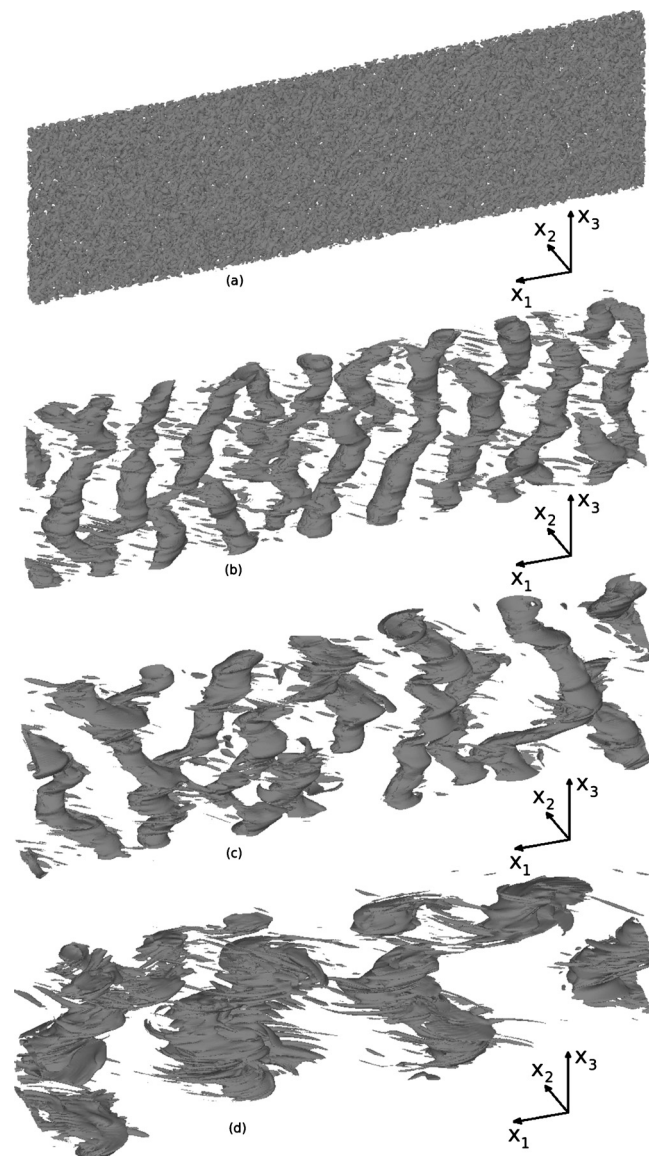


FIG. 10. $\lambda_2 = -0.01$ isosurface contours from the strongly stratified case (A3) showing (a) initial unorganized fluctuations at $t=0$, (b) formation of quasivertical vortical structures at $t=28.5$, (c) vertical shearing of the structures at $t=58.4$, and finally (d) a field of dislocated vortex cores at $t=121.6$.

oriented Gaussian vortex with similar size and circulation to the vortices present in the shear layer, and the coherent structures did not develop structure similar to that observed in Fig. 11(a). This suggested that the interaction of multiple vortices plays a significant, if not necessary role in the development of the three-dimensional structures observed in the present case of horizontal, inflectional shear. Additionally, the deformation of the coherent structures is likely driven by a process similar to the zigzag instability or simply the growth of three-dimensional fluctuations with wavelength $k_3 < N/U_0$ as predicted in Deloncle *et al.*¹⁵ via the kinematic decorrelation mechanism of Lilly.²⁹ However, we conclude that the initial quasivertical orientation of the vortices alone cannot explain the evolution of coherent structures through mechanisms similar to those observed during the instability of a quasivertical vortex.²¹

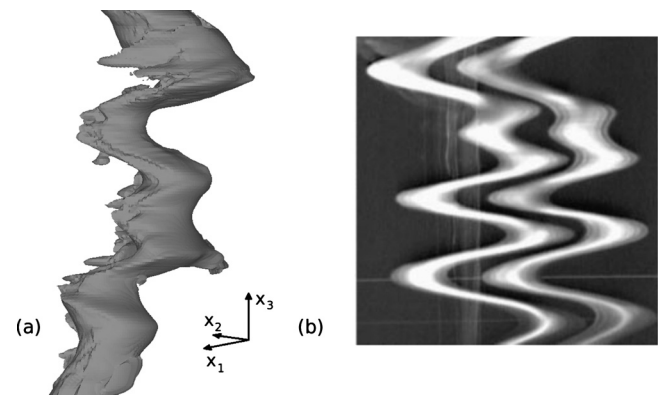


FIG. 11. (a) Coherent structure isolated using an isocontour of $\lambda_2 = -0.01$ at $t=58.4$ and (b) experimental observations of the zigzag instability (Ref. 17).

D. Statistics conditioned on vortical structures

Statistics were computed on flow variables conditioned on the λ_2 criterion to determine the role of spatially sparse coherent structures in the statistical evolution of the model problem. Figure 12 shows the volume fraction and area fraction of the coherent structures as a function of x_2 , showing that structures are primarily confined in the region where $|x_2| < \delta_\omega/2$. A small negative threshold, $\epsilon_{th} = -0.01$, was chosen so that the regions of the flow field where $\lambda_2 < \epsilon_{th}$ could confidently be labeled coherent vortical structures. Case A3 was analyzed because of the high level of coherence in the vorticity field in this case, limiting the role of fine scale turbulent structure on dynamics. Figures 13, 15, and 16 show statistics from case A3 computed on full flow fields, coherent regions where $\lambda_2 < \epsilon_{th}$, and incoherent regions where $\lambda_2 > \epsilon_{th}$.

Figure 13 shows the normal Reynolds stresses, $\langle u'_1 u'_1 \rangle$ and $\langle u'_2 u'_2 \rangle$ have greater magnitudes in the vortical structures than in the ambient surroundings. $\langle u'_1 u'_1 \rangle$ takes large values around one vorticity thickness away from the center of the shear layer, far outside of the region containing coherent vorticity. This is due to the laterally propagating density intrusions that contain thin vortical structures in the braid region, which are captured by λ_2 as seen in Fig. 10(d). As the intrusions propagate away from the region of strong shear, their streamwise velocity relatively becomes small compared to their surroundings giving rise to large deviations from the average velocity.

Additionally, we observe large $\langle u'_3 u'_3 \rangle$ inside of the vortical structures, which is due to the tilting of the segments of coherent structures away from vertical orientation via baroclinic torque. Vertical velocities were more strongly confined to the vortical structures in the small amplitude case $A3_{low}$ showing that the structures are responsible for generating vertical velocities in the shear layer. The change in sign of conditioned $\langle u'_1 u'_2 \rangle$, where $x_2 = \pm \delta_\omega/2$, corresponds to the regions outside of the vortex cores containing only braid structures. Figure 14 shows the conditioned Reynolds stresses and turbulent dissipation for the 2D case. Results are similar to case A3 with the exception of the fact that conditioned $\langle u'_1 u'_2 \rangle$ does not take large positive values, likely due

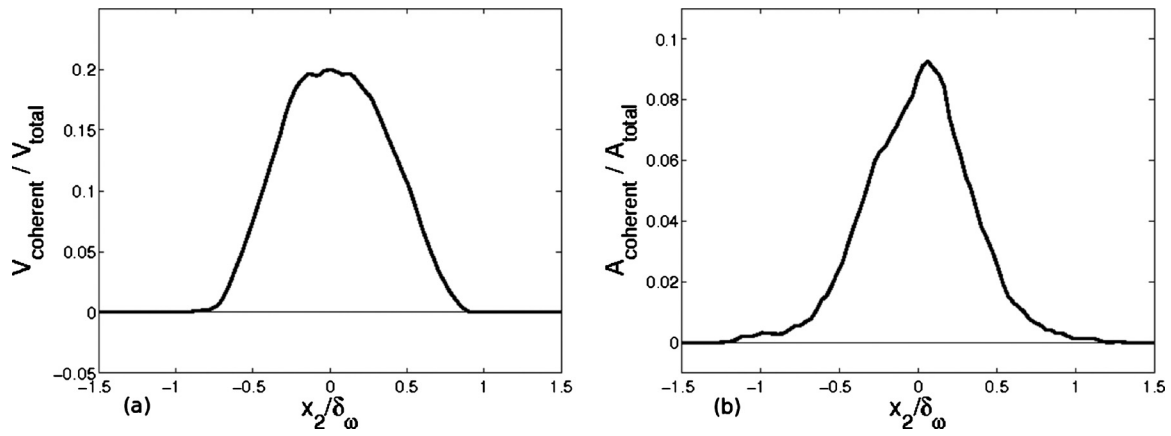


FIG. 12. (a) Volume fraction of flow domain selected as coherent for vertical slices centered at the given values of x_2 , where $\epsilon_{\text{th}} = -0.01$ and $Nr = 87.45$. (b) Area fraction of flow domain selected as coherent for slices at given values of x_2 , where $\epsilon_{\text{th}} = -0.01$ and where $t = 49.46$.

to the fact that buoyancy does not affect the braids that tend to possess significant turbulent potential energy (TPE) in case A3.

In Fig. 15(a), dissipation of TKE is significantly larger within the vortical structures due to the large vertical gradients in the vorticity fields at dislocations that are captured by λ_2 as coherent regions of the flow field. The buoyancy flux is large within the structures, consistent with the collapse of tilting structures providing a mechanism for transfer from

potential to kinetic energy near the x_2 midplane. Conditioned buoyancy flux has a similar shape to the buoyancy flux of the whole field except with a larger amplitude. This illustrates the importance of vortex dynamics to the exchange of kinetic and potential energies in this flow.

Figure 15(c) shows that lateral transport is large in the region outside of the coherent vortices. An approximate balance of turbulent and pressure transport is observed within the structures near the centerline. Conditioned transport

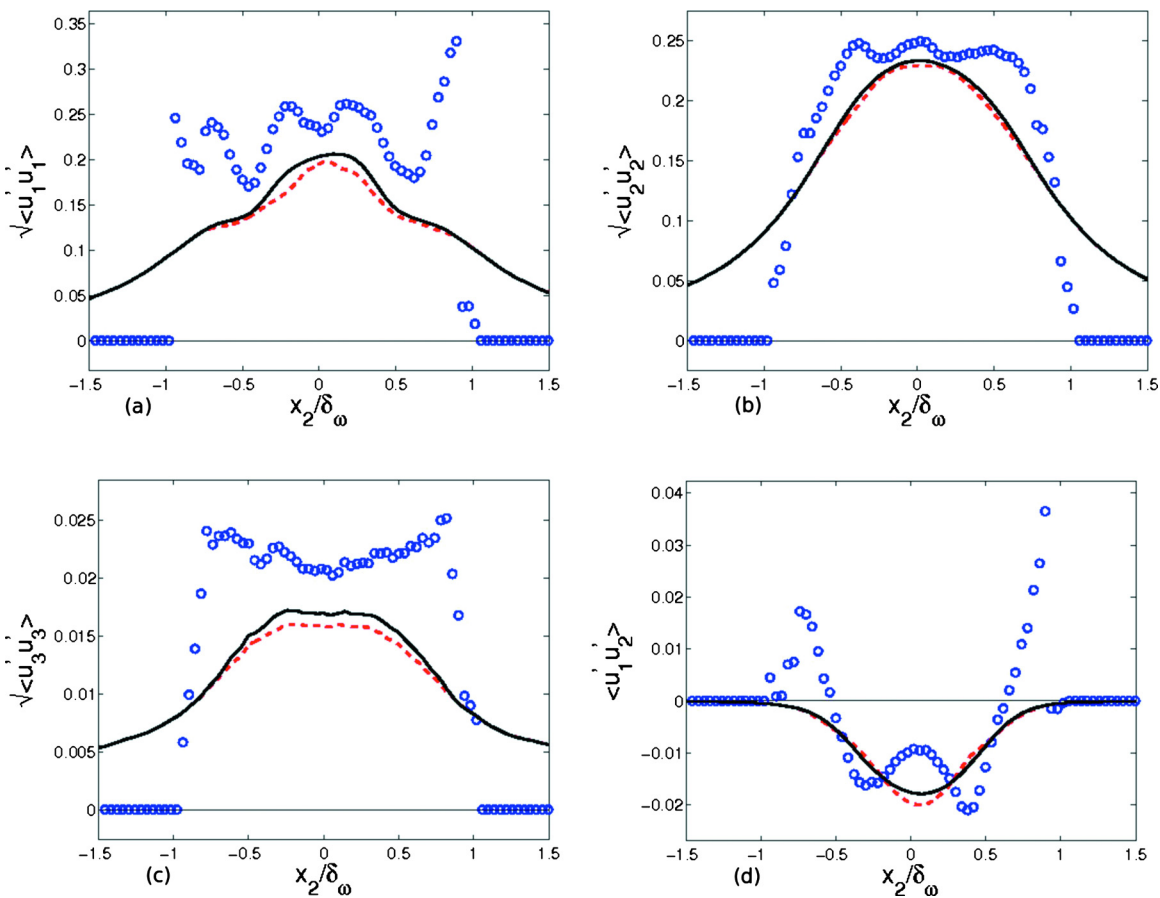


FIG. 13. (Color online) Conditioned energetics from the strongly stratified case (A3) at time $Nr = 87.45$ showing statistics conditioned on vortical structures (circles), full field statistics (solid lines), and statistics conditioned on regions outside of vortical structures (dashed lines), where $\epsilon_{\text{th}} = -0.01$.

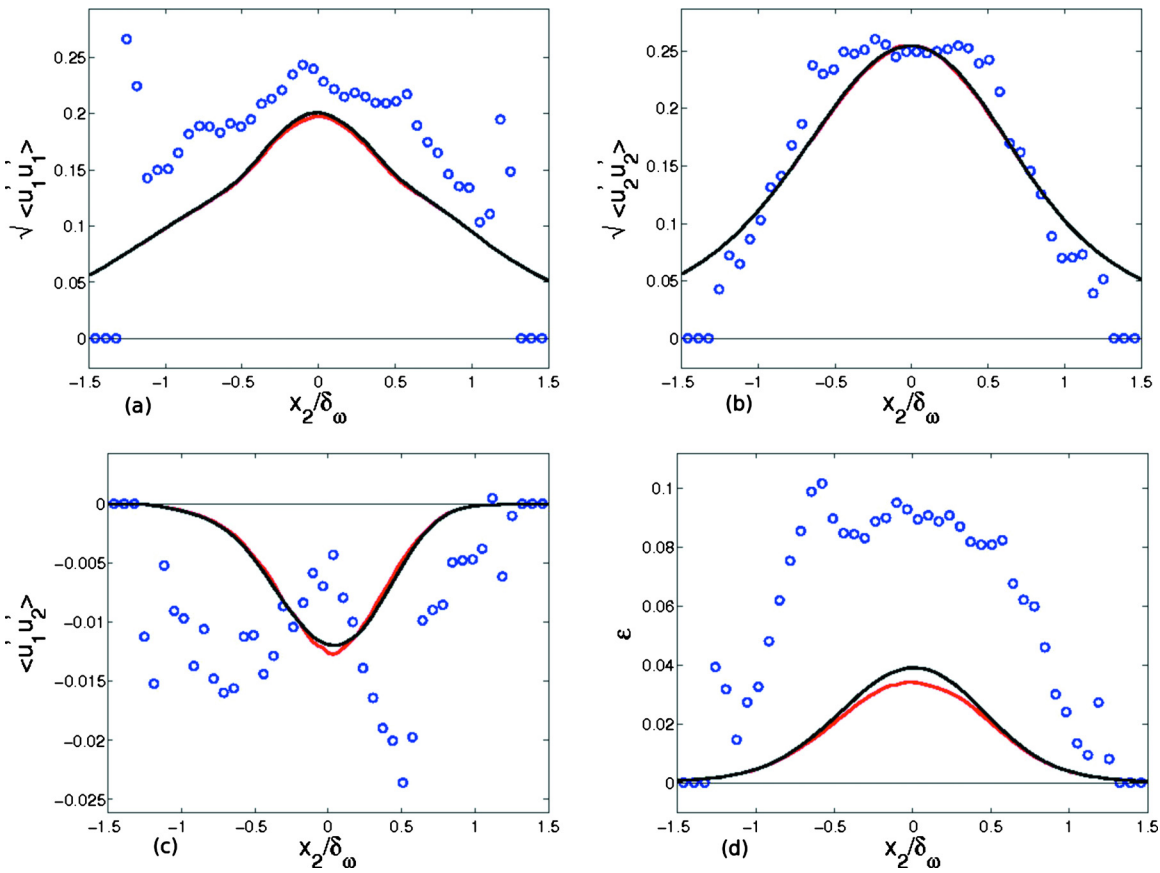


FIG. 14. (Color online) Conditioned energetics from the two-dimensional (2D) case at time $t=49.46$ showing statistics conditioned on vortical structures (circles), full field statistics (dark lines), and statistics conditioned on regions outside of vortical structures (light lines).

strongly suggests that there is net transport of TKE into the coherent structures from the ambient flow field, even when overall transport is directed away from the structures.

In Fig. 16(a), conditioned $\langle \rho' \rho' \rangle$ shows that density fluctuations, and hence fluctuating potential energy gather in the vortical structures. The density variance is large inside of the vortical structures largely due to the presence of pressure minima at the center of the vortex cores that distort isopycnals vertically toward the low pressure region along the central axis of the structures. In Fig. 16(b), greater values of scalar transport are observed in the coherent regions. Integrating the difference between the scalar transport of the full

field and regions outside of the structures indicate that there is a net transfer of scalar fluctuations into the structures from the ambient flow. Figure 16(c) shows that scalar gradients are also concentrated within the coherent structures.

The coherent field occupies a small subset of the computational domain, roughly 2% by volume in case A3 when $Nt=87.45$. Because of this, statistics conditioned on the incoherent field do not significantly differ from the statistics of the full field. Nevertheless, the vortical structures carry significant fluxes, playing an important role in the evolution of the shear layer.

In the interest of developing tractable models to describe

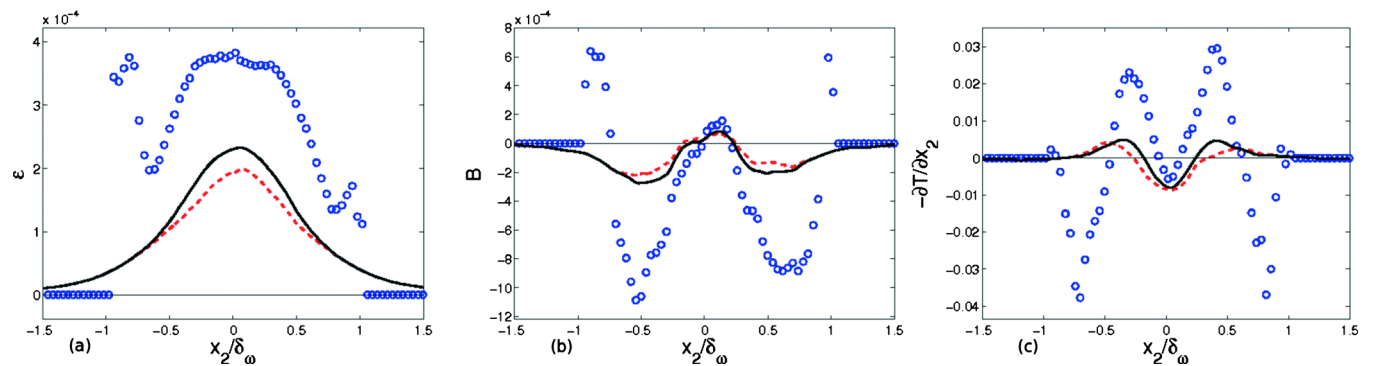


FIG. 15. (Color online) Conditioned energy budget terms from the strongly stratified case (A3) at time $Nt=87.45$ showing statistics conditioned on vortical structures (circles), full field statistics (solid lines), and statistics conditioned on regions outside of vortical structures (dashed lines), where $\epsilon_{th}=-0.01$.

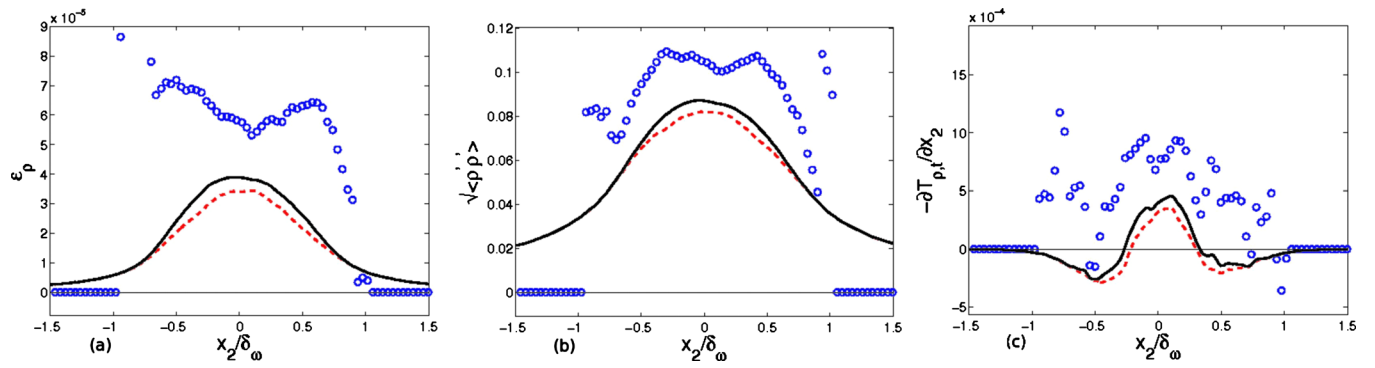


FIG. 16. (Color online) Conditioned scalar statistics from the strongly stratified case (A3) at time $Nt=87.45$ showing statistics conditioned on vortical structures (circles), full field statistics (solid lines), and statistics conditioned on regions outside of vortical structures (dashed lines), where $\epsilon_{th}=-0.01$.

the evolution of geophysical flows dominated by coherent vortical structures, the importance of vorticity contained within the coherent structures was quantified. Flow outside of coherent regions was assumed irrotational and velocities were computed using the Biot–Savart law. The resulting velocity field poorly matched the true field, yielding large relative errors in energetic and mean profiles.

The coherent regions only contained 16.6% of the integrated vorticity magnitude and 39.1% of the integrated enstrophy in the flow when $\epsilon_{th}=-0.01$. Relaxing the threshold by a factor of 100 increased these values to 36.4% and 60.1%, respectively. The vorticity outside of the structures is significant and dynamically important, which does not bode well for the use of simple vortex-based models in geophysical flows.

E. Wavelet analysis

Wavelet-based feature extraction was also used to separate the vorticity field into a coherent field and random incoherent field. By coherent field, we do not imply spatially coherent vortical structures as identified by vortex eduction, but rather a denoised vorticity field. Coiflet wavelets were used with six vanishing moments. The vorticity field was decomposed into coherent and incoherent components as follows:

$$\tilde{\omega}_i = \tilde{\omega}_{C,i} + \tilde{\omega}_{I,i}, \quad (24)$$

where coherent vorticity contains all wavelet coefficients with magnitudes greater than the threshold ϵ_D , where $\epsilon_D = \sqrt{\frac{2}{3} \langle \omega_{I,i}^2 \rangle} \ln \tilde{N}$. Here, \tilde{N} represents the number of computational points on which the wavelet transform is performed. This threshold is used in Jacobitz *et al.*³² and motivated by theorems related to denoising theory.³³ An iterative process is used in the computation of ϵ_D , since $\omega_{I,i}$ is dependent on ϵ_D and vice versa. Once the vorticity fields were split, velocity fields were computed by solving the Poisson equation below

$$\frac{\partial^2 u_i}{\partial x_j \partial x_j} = -\epsilon_{ijk} \frac{\partial \omega_k}{\partial x_j}. \quad (25)$$

Figure 17 shows $\langle u'_1 u'_1 \rangle$, $\langle u'_2 u'_2 \rangle$, fluctuating transport, and

fluctuating dissipation as computed on velocity fields corresponding to the full, coherent, and incoherent vorticity fields. The contribution of incoherent vorticity is negligible. The incoherent vorticity field induces a velocity field with fluctuations two orders of magnitude smaller than those induced by the full vorticity field, and peak turbulent transport magnitude in the incoherent field is five orders of magnitude smaller than the full field.

Prior investigations into homogeneous turbulence show that coherent vorticity can be captured with approximately 3% of the total wavelet coefficients.^{26,32} In the inhomogeneous shear layer, a considerably smaller fraction of wavelet coefficients is needed. The fraction scales with δ_ω to reflect the effect of shear layer growth on degrees of freedom. In case A3 when $\delta_\omega=5.48$, only 0.346% of wavelet coefficients is required to represent the coherent field. The fraction of coefficients deemed coherent decreases as stratification increases, with case A0 having an order of magnitude greater coherent coefficients than case A3 at comparable values of δ_ω .

Vortex eduction was performed on the coherent field in case A3 using the λ_2 criterion. The result was almost identical to that on the full field. The dissipation, including the patches with high value, was also accurately represented with the coherent field.

VIII. CONCLUSIONS

The statistical evolution of a mixing layer where the mean shear, $\partial \langle u_1 \rangle / \partial x_2$, is horizontal was investigated for a range of stratifications and the role of coherent structures clarified. The statistics significantly vary between cases with different levels of stratification. Many statistics could be collapsed between cases when times corresponding the same $Ri_b(t)$ were chosen. This dependence on $Ri_b(t)$ disappeared at late time in the strongly stratified cases where $Ri_b \gg 1$ leads to approximately self-similar evolution in some statistics such as turbulent stresses. In the self-similar state, the turbulent stresses were similar to those in two-dimensional shear layers. However, the turbulent dissipation rate was significantly larger in the stratified shear layer in comparison with

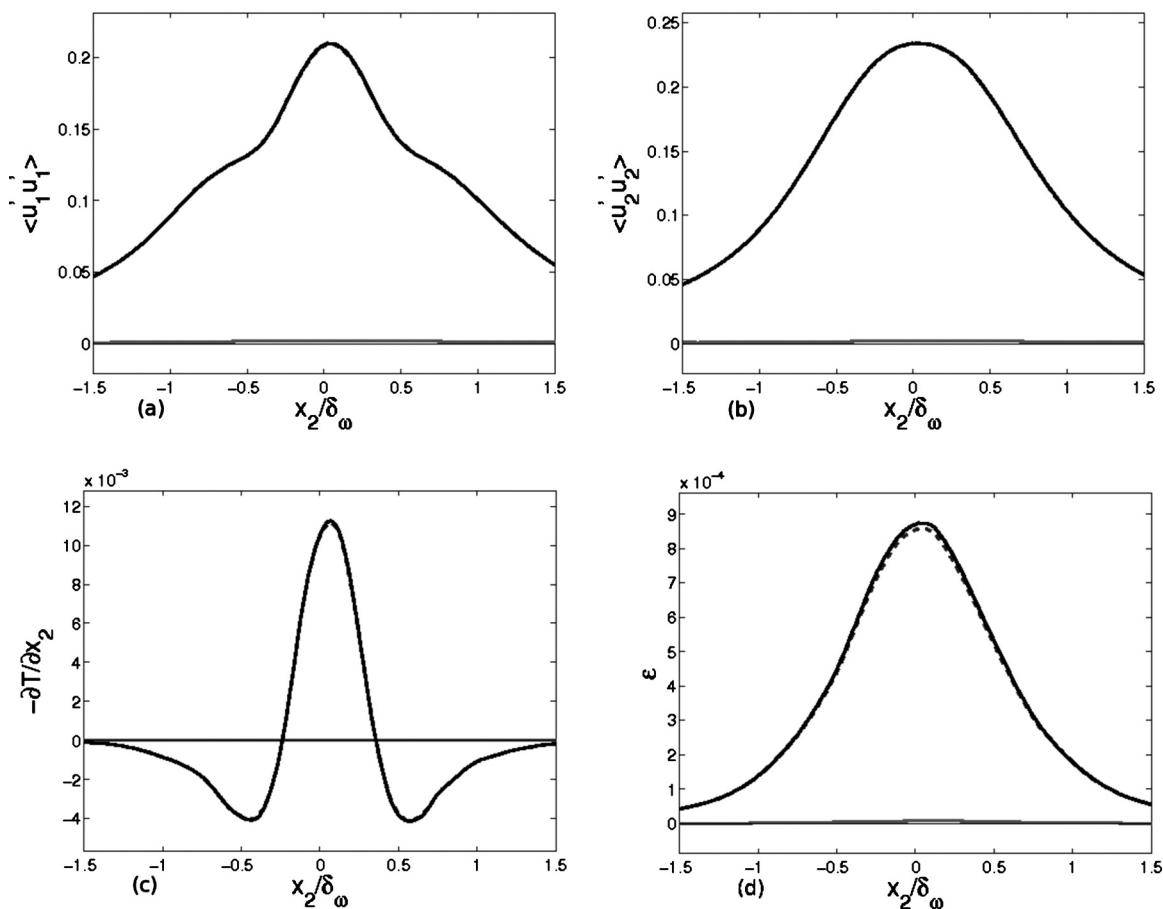


FIG. 17. Statistics from the strongly stratified case (A3) at time $Nt=76.76$ showing statistics corresponding to full vorticity (solid dark), coherent vorticity (dashed dark), and incoherent vorticity (solid light), where $\epsilon_D=0.262$.

the two-dimensional case. Buoyancy leads to important processes not observed in the unstratified and two-dimensional simulations such as density intrusions, tilting and collapsing vortical structures and vertical slicing similar to the zigzag instability.

Stratification was found to decrease dissipation levels and increase lateral spread of turbulence leading to higher shear layer growth rates. When density behaved as an active scalar, significant countergradient transport of density fluctuations was observed in the central region, which was fundamentally different from the passive scalar case's cogradient transport.

While in a vertical stratified shear layer intense vertical mixing can be accomplished during the mixing transition, which is short-lived, vertical mixing can occur in the horizontal shear layer over longer time periods. Strong vertical gradients are introduced through secondary instabilities that induce dislocations in coherent structures with vertical vorticity. The zigzag instability, shown earlier in the case of a counter-rotating vortex pair, may be the slicing mechanism observed in the present problem with horizontal shear after coherent vortices emerge from the initial turbulence.

Spatially coherent vortical structures were identified using the λ_2 criterion. The influence of these vortical structures on the evolution of the mixing layer was discussed. Vortical structures play important roles in the coupling of scalar and

velocity fields and contain concentrations of kinetic and potential energies. The exchange between coherent and ambient flow is significant and energy transport is primarily accomplished by the ambient flow. Irreversible losses to viscous and scalar dissipation are also concentrated within the coherent structures. However, the domain outside the identified vortex structures also contains significant vorticity. Therefore, statistics conditioned on the coherent structures do not agree with the full statistics. The importance of the ambient vorticity on statistical evolution is a surprising result of this work.

Wavelet analysis of the vorticity field shows that significant reduction in the number of degrees of freedom is possible when modeling or simulating stratified turbulence. The incoherent vorticity field is found to have negligible effect on the statistics and the coherent vortical structures, even though it contains well over 99% of the wavelet modes. The incoherent field plays a less significant role in the stratified cases than in the unstratified case.

ACKNOWLEDGMENTS

The authors are pleased to acknowledge partial support by the Jacobs School Graduate Fellowship (for E.A.) and the National Science Foundation CDI program through Grant No. OCE-0835839 (for S.S. and E.A.).

- ¹S. A. Thorpe, "On the shape and breaking of finite amplitude internal gravity waves in a shear flow," *J. Fluid Mech.* **138**, 185 (1984).
- ²C. G. Koop and F. K. Browand, "Instability and turbulence in a stratified fluid with shear," *J. Fluid Mech.* **93**, 135 (1979).
- ³W. D. Smyth and J. N. Moum, "Length scales of turbulence in stably stratified mixing layers," *Phys. Fluids* **12**, 1327 (2000).
- ⁴W. D. Smyth and J. N. Moum, "Anisotropy of turbulence in stably stratified mixing layers," *Phys. Fluids* **12**, 1343 (2000).
- ⁵W. D. Smyth, J. N. Moum, and D. R. Caldwell, "The efficiency of mixing in turbulent patches: Inferences from direct simulations and microstructure observations," *J. Phys. Oceanogr.* **31**, 1969 (2001).
- ⁶E. J. Strang and H. J. S. Fernando, "Entrainment and mixing in stratified shear flows," *J. Fluid Mech.* **428**, 349 (2001).
- ⁷W. R. Peltier and C. P. Caulfield, "Mixing efficiency in stratified shear flows," *Annu. Rev. Fluid Mech.* **35**, 135 (2003).
- ⁸K. L. Tse, A. Mahalov, B. Nicolaenko, and H. J. S. Fernando, "Quasi-equilibrium dynamics of shear-stratified turbulence in a model tropospheric jet," *J. Fluid Mech.* **496**, 73 (2003).
- ⁹H. Pham, S. Sarkar, and K. A. Brucker, "Dynamics of a stratified shear layer above a region of uniform stratification," *J. Fluid Mech.* **630**, 191 (2009).
- ¹⁰H. Pham and S. Sarkar, "Internal waves and turbulence in a stable stratified jet," *J. Fluid Mech.* **648**, 297 (2010).
- ¹¹F. G. Jacobitz and S. Sarkar, "The effect of nonvertical shear on turbulence in a stably stratified medium," *Phys. Fluids* **10**, 1158 (1998).
- ¹²F. G. Jacobitz and S. Sarkar, "A direct numerical study of transport and anisotropy in a stably stratified turbulent flow with uniform horizontal shear," *Flow, Turbul. Combust.* **63**, 343 (2000).
- ¹³S. Basak and S. Sarkar, "Dynamics of a stratified shear layer with horizontal shear," *J. Fluid Mech.* **568**, 19 (2006).
- ¹⁴W. Blumen, "Hydrostatic neutral waves in a parallel shear flow of a stratified fluid," *J. Atmos. Sci.* **28**, 340 (1971).
- ¹⁵A. Deloncle, J.-M. Chomaz, and P. Billant, "Three-dimensional stability of a horizontally sheared flow in a stably stratified fluid," *J. Fluid Mech.* **570**, 297 (2007).
- ¹⁶C. D. Winant and F. K. Browand, "Vortex pairing: The mechanism of turbulent mixing-layer growth at moderate Reynolds number," *J. Fluid Mech.* **63**, 237 (1974).
- ¹⁷P. Billant and J.-M. Chomaz, "Experimental evidence for a new instability of a vertical columnar vortex pair in a strongly stratified fluid," *J. Fluid Mech.* **418**, 167 (2000).
- ¹⁸P. Billant and J.-M. Chomaz, "Theoretical analysis of the zigzag instability of a vertical columnar vortex pair in a strongly stratified fluid," *J. Fluid Mech.* **419**, 29 (2000).
- ¹⁹M. L. Waite and P. K. Smolarkiewicz, "Instability and breakdown of a vertical vortex pair in a strongly stratified fluid," *J. Fluid Mech.* **606**, 239 (2008).
- ²⁰A. Deloncle, P. Billant, and J. M. Chomaz, "Nonlinear evolution of the zigzag instability in stratified fluids: A shortcut on the route to dissipation," *J. Fluid Mech.* **599**, 229 (2008).
- ²¹N. Boulanger, P. Meunier, and S. Le Dizès, "Structure of a stratified tilted vortex," *J. Fluid Mech.* **583**, 443 (2007).
- ²²M. S. Chong, A. E. Perry, and B. J. Cantwell, "A general classification of three-dimensional flow fields," *Phys. Fluids A* **2**, 765 (1990).
- ²³J. Jeong and F. Hussain, "On the identification of a vortex," *J. Fluid Mech.* **285**, 69 (1995).
- ²⁴P. Chakraborty, S. Balachandar, and R. J. Adrian, "On the relationships between local vortex identification schemes," *J. Fluid Mech.* **535**, 189 (2005).
- ²⁵G. Haller, "An objective definition of a vortex," *J. Fluid Mech.* **525**, 1 (2005).
- ²⁶M. Farge, G. Pellegrino, and K. Schneider, "Coherent vortex extraction in 3D turbulent flows using orthogonal wavelets," *Phys. Rev. Lett.* **87**, 054501 (2001).
- ²⁷C. Pantano and S. Sarkar, "A study of compressibility effects in the high-speed turbulent shear layer using direct simulation," *J. Fluid Mech.* **451**, 329 (2002).
- ²⁸P. Billant and J.-M. Chomaz, "Self-similarity of strongly stratified inviscid flows," *J. Fluid Mech.* **13**, 1645 (2001).
- ²⁹D. K. Lilly, "Stratified turbulence and the mesoscale variability of the atmosphere," *J. Atmos. Sci.* **40**, 749 (1983).
- ³⁰J. J. Riley and S. M. deBruynKops, "Dynamics of turbulence strongly influenced by buoyancy," *Phys. Fluids* **15**, 2047 (2003).
- ³¹R. R. Kerswell, "Elliptical instability," *Annu. Rev. Fluid Mech.* **34**, 83 (2002).
- ³²F. G. Jacobitz, L. Liechtenstein, K. Schneider, and M. Farge, "On the structure and dynamics of sheared and rotating turbulence: Direct numerical simulation and wavelet-based coherent vortex extraction," *Phys. Fluids* **20**, 045103 (2008).
- ³³D. L. Donoho and J. M. Johnstone, "Ideal spatial adaptation by wavelet shrinkage," *Biometrika* **81**, 425 (1994).